Journal of Biomedical Optics

BiomedicalOptics.SPIEDigitalLibrary.org

Photoacoustic imaging to assess pixel-based sO_2 distributions in experimental prostate tumors

Alina L. Bendinger
Christin Glowa
Jörg Peter
Christian P. Karger

SPIE.

Alina L. Bendinger, Christin Glowa, Jörg Peter, Christian P. Karger, "Photoacoustic imaging to assess pixel-based sO_2 distributions in experimental prostate tumors," *J. Biomed. Opt.* **23**(3), 036009 (2018), doi: 10.1117/1.JBO.23.3.036009.

Photoacoustic imaging to assess pixel-based sO_2 distributions in experimental prostate tumors

Alina L. Bendinger,[a,b,*] Christin Glowa,[c,d,e] Jörg Peter,[a] and Christian P. Karger[c,e]
[a]German Cancer Research Center, Department of Medical Physics in Radiology, Heidelberg, Germany
[b]University of Heidelberg, Faculty of Biosciences, Heidelberg, Germany
[c]German Cancer Research Center, Department of Medical Physics in Radiation Oncology, Heidelberg, Germany
[d]University Hospital Heidelberg, Department of Radiation Oncology and Radiotherapy, Heidelberg, Germany
[e]Heidelberg Institute for Radiation Oncology, National Center for Radiation Research in Oncology, Heidelberg, Germany

Abstract. A protocol for photoacoustic imaging (PAI) has been developed to assess pixel-based oxygen saturation (sO_2) distributions of experimental tumor models. The protocol was applied to evaluate the dependence of PAI results on measurement settings, reproducibility of PAI, and for the characterization of the oxygenation status of experimental prostate tumor sublines (Dunning R3327-H, -HI, -AT1) implanted subcutaneously in male Copenhagen rats. The three-dimensional (3-D) PA data employing two wavelengths were used to estimate sO_2 distributions. If the PA signal was sufficiently strong, the distributions were independent from signal gain, threshold, and positioning of animals. Reproducibility of sO_2 distributions with respect to shape and median values was demonstrated over several days. The three tumor sublines were characterized by the shapes of their sO_2 distributions and their temporal response after external changes of the oxygen supply (100% O_2 or air breathing and clamping of tumor-supplying artery). The established protocol showed to be suitable for detecting temporal changes in tumor oxygenation as well as differences in oxygenation between tumor sublines. PA results were in accordance with histology for hypoxia, perfusion, and vasculature. The presented protocol for the assessment of pixel-based sO_2 distributions provides more detailed information as compared to conventional region-of-interest-based analysis of PAI, especially with respect to the detection of temporal changes and tumor heterogeneity. [DOI: 10.1117/1.JBO.23.3.036009]

Keywords: photoacoustic imaging; oxygen saturation; tumor hypoxia; rat prostate tumor R3327.

Paper 170719R received Nov. 7, 2017; accepted for publication Feb. 19, 2018; published online Mar. 20, 2018.

1 Introduction

Photoacoustic imaging (PAI) is an emerging noninvasive imaging technique attracting increasing attention for preclinical and clinical applications in various fields.[1–3] Without ionizing radiation, PAI combines high contrast and specificity of optical imaging with high spatial resolution of ultrasound (US) imaging.[2,4] Briefly, locally absorbed laser energy leads to an increase in temperature and a rapid thermoelastic expansion of the heated tissue. The resulting pressure wave then propagates through the tissue and is detected by an US transducer at the surface of the body.[4,5] Tissue comprises several endogenous chromophores, such as hemoglobin and melanin, which exhibit characteristic wavelength-dependent absorption spectra. This causes contrast in PAI without the need of exogenous contrast agents.[4]

Tumor hypoxia and changes in tumor oxygen content are important factors, especially with respect to treatment response.[6] Various modalities are available for monitoring hypoxia, such as hypoxia-specific positron emission tomography tracers, Eppendorf-electrodes, and magnetic resonance imaging-based methods, however, all come along with specific limitations.[6,7] Noninvasiveness, lack of ionizing radiation, as well as high contrast and specificity are hallmarks of PAI promising a high potential for *in vivo* assessment of oxygen saturation (sO_2) in preclinical and, nowadays, clinical studies.[8] While deoxygenated and oxygenated hemoglobin can be directly distinguished by PAI based on their absorption patterns, sO_2 can be calculated by using laser light of different wavelengths.[9]

Commercial PAI systems often only allow the evaluation of mean values of predefined regions of interest (ROI). However, tumors often exhibit highly heterogeneous structures, especially with respect to oxygenation. Hence, we aimed for an analysis that reflects this inter- and intratumor heterogeneity by representing all pixels' information in distributions.

In this study, we developed and tested a protocol to assess pixel-based sO_2 distributions of entire tumor volumes. The method was applied to three sublines of an experimental prostate carcinoma to demonstrate suitability, sensitivity, and feasibility of the method to detect acute changes in oxygenation.

2 Materials and Methods

2.1 *Tumor Model*

All experiments were approved by the governmental review committee on animal care, and animals were kept under standard laboratory conditions.

Fresh fragments of tumor tissue of the experimental prostate adenocarcinoma sublines Dunning R3327-H, -HI, and -AT1[10] were implanted subcutaneously in the distal right thigh of adult male Copenhagen rats (Charles River Laboratories Inc., Wilmington, Massachusetts). The well differentiated and hormone-sensitive H-tumor grows slowly with a volume doubling

*Address all correspondence to: Alina L. Bendinger, E-mail: a.bendinger@dkfz-heidelberg.de

1083-3668/2018/$25.00

time (VDT) of ~20 days, while the differentiated but hormone-independent HI-tumor exhibits a VDT of ~10 days. The anaplastic AT1-tumor is hormone-independent showing a VDT of ~5 days.[11]

During PAI, animals were anaesthetized with a mixture of 3% sevoflurane (Abbvie, Ludwigshafen, Germany) and air (ambient condition) at 1.0 l/min if not stated differently. Animals were positioned on a heatable table, and ECG and respiration rate were monitored during imaging.

2.2 *Photoacoustic Imaging*

Prior to PAI, the animals' skin was thoroughly depilated by hair removal creme. Animals were placed on the heatable table and US gel was generously applied on the entire tumor volume surface. The present study was conducted with the commercial systems Vevo 2100 and Vevo 3100 (both Fujifilm VisualSonics Inc., Toronto, Canada) using a tunable Nd:YAG laser (Vevo LAZR, Fujifilm VisualSonics Inc.). The laser emits photons at a 20-Hz pulse rate with a peak energy of ~30 mJ and 10 ns length.[12] Imaging was performed with the system-specific linear-array US transducers exhibiting a center frequency of 21 MHz (transducer LZ250 for Vevo 2100, transducer MX250 for Vevo 3100; both Fujifilm VisualSonics Inc.). For detection of deoxygenated and oxygenated hemoglobin, two excitation wavelengths (750 and 850 nm) were used. The PAI system was calibrated before each imaging session.

Settings for time gain compensation and signal gain were optimized for each measurement using the hemoglobin signal in the "HemoMeaZure" mode of the Vevo imaging software (Fujifilm, VisualSonics Inc.) to obtain a homogeneous signal distribution over the entire tumor. All PAI data were acquired in three-dimensional (3-D) "oxy-hemo" mode (Vevo imaging software) with a step size of 0.15 mm and low persistence if not stated differently. Tumor volumes were determined based on simultaneously acquired US B-mode images in VevoLab software (Fujifilm VisualSonics Inc.).

2.3 *Image Processing and Analysis*

A protocol has been developed to assess pixel-based sO_2 distributions over the entire 3-D tumor volumes using the beam-formed raw data of the signals at 750 and 850 nm, respectively. In the following, the measurement protocol is summarized.

I. Data filtering: A 3-D Gaussian filter (2 sigma) was applied to the beam-formed PA raw data for both wavelengths using the image processing software ImageJ.[13]

II. Oxygen saturation calculation: sO_2 was calculated pixel-wise from the PA signal at the corresponding wavelengths (PA_λ) using the molar extinction coefficients of deoxygenated and oxygenated hemoglobin ($\varepsilon^{\lambda}_{\mathrm{Hb}}$ and $\varepsilon^{\lambda}_{\mathrm{HbO_2}}$, respectively[14]) according to

$$sO_2 = \frac{[HbO_2]}{[HbO_2] + [Hb]} = \frac{PA_{\lambda_2}\varepsilon^{\lambda_1}_{\mathrm{Hb}} - PA_{\lambda_1}\varepsilon^{\lambda_2}_{\mathrm{Hb}}}{PA_{\lambda_1}\Delta\varepsilon^{\lambda_2}_{\mathrm{Hb}} - PA_{\lambda_2}\Delta\varepsilon^{\lambda_1}_{\mathrm{Hb}}}, \quad (1)$$

where $\Delta\varepsilon_{\mathrm{Hb}} = \varepsilon_{\mathrm{HbO_2}} - \varepsilon_{\mathrm{Hb}}$[9] using MATLAB R2016a (MathWorks, Inc. Natick, Massachusetts). For each tumor, this procedure was repeated for each frame of the 3-D image stack.

III. Data thresholding: The hemoglobin image was calculated in VevoLab[12] and was then converted into a likelihood-map representing the probability that the signal of one pixel originated from hemoglobin. If the probability of any given pixel in the likelihood-map was below a predefined threshold, the respective pixel in the sO_2 image was set to zero and was excluded from further analysis.

IV. Region of interest analysis: Tumor ROIs were delineated manually according to simultaneously acquired US B-mode images.

V. sO_2-histogram derivation: The sO_2 distributions within the ROIs were condensed into normalized histograms using a bin size of 0.5%. For comparison of sO_2 distributions, the median as well as the 25th and 75th percentiles (25/75) were extracted. Due to measurement uncertainty and noise, some of the measured sO_2 distributions showed a negligible amount of histogram entries above 100% sO_2.

VI. Earth mover's distance calculation: To quantify the similarity of two histograms, the Earth mover's distance (EMD),[15–17] a recognized measure of distance between two probability distributions,[18] was calculated. It represents the minimal cost of transferring one distribution into another, when the cost is defined as the sum of the histogram entries times the distance they have to be moved.[19] Recently, it has also been applied in various fields of biological and medical research.[20–22] For the present application in PAI, the EMD can be expressed as follows:

$$\mathrm{EMD} = \int_{-\infty}^{\infty} |F_a(x) - F_b(x)|dx, \quad (2)$$

where $F_a(x)$ and $F_b(x)$ are the cumulative distribution functions of the probability densities a and b, respectively.[16] For identical distributions, the EMD is equal to 0, while the maximum EMD is 1, which is only the case for two single-bin histograms located at 0% and 100% sO_2.

2.4 *Dependency of sO_2 Distributions on Signal Gain and Threshold*

Measurements were performed at Vevo 2100 with Vevo-LAZR without persistence. Two animals were imaged with three different signal gains (36 dB, 38 dB, 40 dB). Data were analyzed for three different thresholds (0%, 15%, 30%). Both parameters were selected within a range applicable for *in vivo* measurements. Reproducibility of sO_2 distributions was assessed by repeating this procedure after repositioning of animals. As sO_2 distributions were essentially independent of the settings, all subsequent measurements were performed with an individually adjusted signal gain and a threshold of 20%. All following measurements were performed at the Vevo 3100 with the Vevo-LAZR at low persistence.

2.5 *Characterization of Tumor Sublines and Their Temporal Development*

Two tumors of comparable volumes were imaged per subline (H, HI, AT1) and their sO_2 distributions were pooled. Measurements were repeated at least three times over a period of up to 41 days.

2.6 *Sensitivity of sO_2 Distributions on External Changes in Oxygen Supply*

The animals' breathing gas supply was altered (Fig. 1): animals were sequentially imaged when breathing 100% oxygen (O_2),

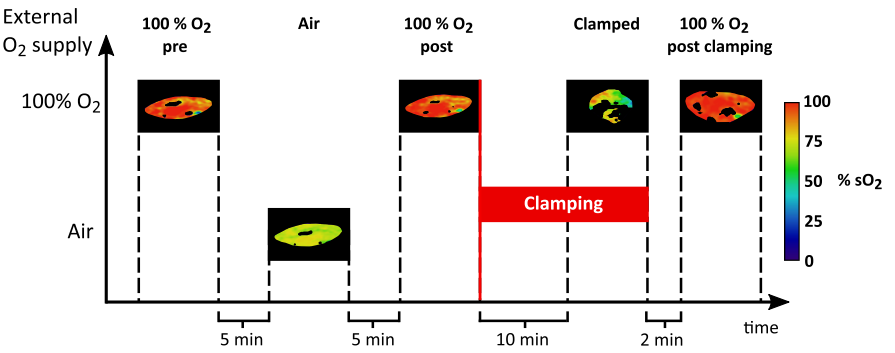

Fig. 1 Schematic illustration of the oxygenation conditions during PA measurements. Color-coded "oxyhemo" images show the same tumor ROI under different experimental conditions.

ambient air, and again 100% O_2. After each alteration of oxygen conditions, a delay of 5 min was added allowing for adaption of the tumor to the new condition. Subsequently, an additional measurement was performed 10 min after clamping the tumor-supplying arteries with a transparent cable retainer, which induces acute hypoxic conditions in the tumors while the animals were still breathing 100% O_2. Immediately thereafter, the cable retainer was removed and the animals were imaged again. This measurement procedure was performed for two tumors per subline. Measurements were repeated at the same time points as the measurement of the temporal development (Sec. 2.5). For comparison with well-oxygenated normal tissue, these measurements were performed also for the skin of two animals.

2.7 *Histology and Immunohistochemistry*

After the final imaging, animals were injected intravenously with pimonidazole hydrochloride (60 mg/kg, Hypoxyprobe™-1 Kit, NPI, Inc., Burlington, Massachusetts). After 1 h, Hoechst 33342 dye (15 mg/kg, Merck, Darmstadt, Germany) was injected as a perfusion marker into the right ventricle of the heart 30 s before sacrificing the animals. Tumors were dissected and stored at −80°C. Tumors were embedded in Tissue Tek (Sakura, Alphen aan den Rijn, the Netherlands), cut into 7-μm thick slices, and fixated in methanol/acetone at −20°C.

For evaluation of tumor tissue structures, cryo sections were stained with hematoxylin/eosin (H&E, Carl Roth GmbH & Co. KG, Karlsruhe, Germany). Briefly, sections were stained with hematoxylin for 5 min and washed in floating tap water for 10 min. Subsequently, they were immersed in eosin (0.5% aqueous solution) for 5 min and rinsed in distilled water before dehydration with ethanol and mounting in Eukitt (Kindler, Freiburg, Germany).

Immunofluorescence stainings were performed for pimonidazole, CD31, and carbonic anhydrase IX (CAIX). Cryo sections were incubated with signal enhancer (Life Technologies, Eugene, Oregon), blocked against unspecific binding (Dako North America, Inc., Carpinteria, California) and subsequently incubated with FITC-labeled mouse antipimonidazole antibody in 3% bovine serum albumin/phosphate buffered saline (BSA/PBS) (1:2000) over night at 4°C. The next day, sections were washed in PBS and incubated at room temperature (RT) with either goat anti-rat CD31 antibody (R&D Systems, Inc., Minneapolis, Minnesota) in 3% BSA/PBS (1:2000) for 1 h or rabbit polyclonal anti-CAIX antibody (Novus Biologicals, Littleton, Colorado) in 3% BSA/PBS (1:1000) for 2 h. After subsequent washing in PBS, sections were stained with donkey anti-goat AlexaFluor-555 antibody (1:3000, Invitrogen, Eugene, Oregon) or goat anti-rabbit AlexaFluor-555 antibody (1:1000, Invitrogen) in 3% BSA/PBS, respectively, at RT for 30 min. Sections were washed in PBS and mounted in Fluoromount® (Dako). All sections were evaluated with an Axio Scan.Z1 microscope (Carl Zeiss Microscopy GmbH, Jena, Germany).

3 Results

3.1 *Dependency of sO_2 Distributions on Signal Gain and Threshold*

Figure 2 and Table 1 display the sO_2 distributions as well as the median and 25/75 percentiles of sO_2 distributions for the different combinations of signal gains and thresholds for two HI-tumors.

The tumor HI-1 exhibited a homogenous PA signal with a clearly detectable skin line. Visual inspection of the normalized sO_2 distributions revealed only minor differences in the shape of the distributions for the different settings (Fig. 2, first and second row). Regarding the 25/75 percentile ranges, the distributions became slightly narrower with increasing threshold, however, without affecting the medians (Table 1). Repeating the imaging procedure after repositioning the animal did not reveal any differences in shape, medians, and 25/75 percentile ranges (Fig. 2 and Table 1). Depending on the signal gain during measurement and threshold during analysis, the number of pixels included into analysis ranged from 40% to 100%.

Tumor HI-2, exhibited a very weak PA signal with a hardly detectable skin line, even at a signal gain of 40 dB. Table 1 reveals that even though medians were not affected, the shape and 25/75 percentile ranges of the sO_2 distributions changed somewhat depending on threshold and signal gain (Fig. 2, third and fourth row): While the histograms at 0% threshold were identical for all signal gains even after repositioning of the animal (Fig. 2 and Table 1), a large variability was observed for higher thresholds, especially in combination with a low signal gain. Under these conditions, only a negligible fraction of pixels with signals near the noise-level could be analyzed (e.g., only 10% of the pixels for all three signal gains at a threshold of 30%).

To obtain reliable and reproducible results, it was therefore important to adjust the measurement settings and especially

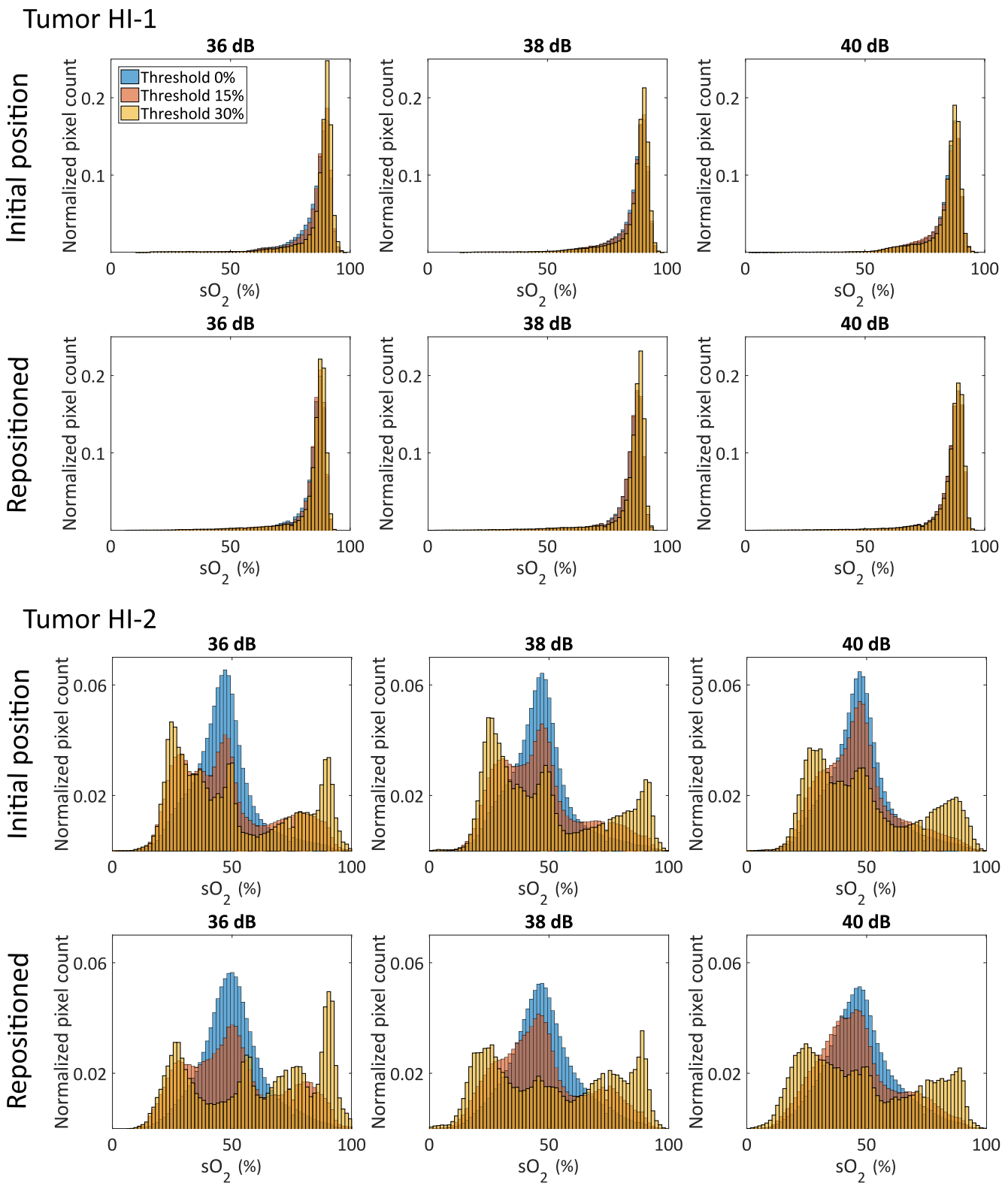

Fig. 2 Normalized sO_2 distributions of two HI-tumors for different signal gains and thresholds for two independent positionings of the animal. The sO_2 distributions of tumor HI-1 were largely independent from signal gain, threshold, and positioning. The animal with the larger tumor HI-2 (rows 3 and 4) only exhibited identical sO_2 distributions for a 0% threshold. With increasing threshold, the variability of the distribution increased due to the very low number of evaluated pixels.

Table 1 Medians and 25/75 percentiles of the sO_2 distributions for the investigated combinations of signal gain and threshold. Values are given for two HI-tumors (small and large volume) and two independent positions of the animal (Repos = second positioning).

Gain (dB)	Threshold (%)	HI-1 (60 mm^3) sO_2 median [25%, 75%]	sO_2 median Repos [25%, 75%]	HI-2 (740 mm^3) sO_2 median [25%, 75%]	sO_2 median Repos [25%, 75%]
36	0	88 [83, 90]	86 [83, 88]	46 [39, 52]	50 [42, 57]
36	15	89 [85, 91]	86 [83, 88]	44 [32, 59]	49 [36, 65]
36	30	90 [87, 91]	87 [84, 89]	44 [29, 74]*	61 [34, 83]*
38	0	88 [84, 91]	86 [83, 88]	46 [38, 52]	47 [39, 56]
38	15	89 [84, 91]	86 [83, 88]	44 [33, 54]	45 [34, 58]
38	30	89 [86, 91]	87 [85, 89]	43 [29, 70]*	50 [27, 76]*
40	0	86 [82, 88]	87 [84, 90]	47 [39, 53]	47 [38, 55]
40	15	86 [81, 89]	87 [84, 90]	45 [35, 53]	44 [35, 55]
40	30	87 [83, 89]	88 [85, 90]	45 [31, 68]*	45 [28, 71]*

*indicates measurements where the percentage of pixels to zero was below 10% resulting in sO_2 distributions, which are not anymore representative for the tumor.

the signal gain individually for each animal and each imaging session. The skin layer had been selected as a reliable reference for those adjustments.

3.2 *Characterization of Tumor Sublines*

Figure 3 displays the pooled sO_2 distributions of two tumors of comparable size per subline while the animals were breathing air. The well oxygenated H-tumor exhibited a narrow and well-defined peak with a median of 73% (25/75 percentile range: 69%/76%). Similarly, the HI-tumor exhibited a median of 71% with a somewhat wider distribution (25/75 percentile range: 62%/76%). By contrast, the distribution of the AT1-tumor was located around a median of 40% and exhibited a different shape, however, with a comparable 25/75 percentile range (34%/47%).

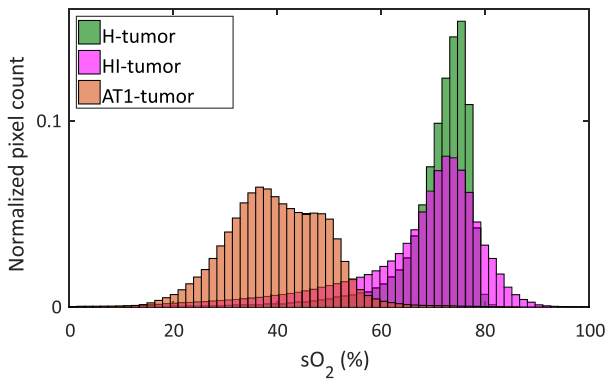

Fig. 3 Pooled sO_2 distributions of two tumors per subline while animals were breathing air. The sublines show clearly distinguishable sO_2 distributions.

3.3 *Temporal Development*

PAI was repeated several times over a period of up to 41 days and as an example, sO_2 distributions at different time points are displayed in Figs. 4(a)–4(c). Median values and 25/75 percentiles for all measurement time points are provided in Table 2.

Repeating the measurement, the tumor H-2 [Fig. 4(a)] essentially maintained the shape of the distribution; however, the distributions shifted slightly toward lower sO_2 values with time. During the observation period, the volume of this tumor did not change [Fig. 4(d)]. For tumor H-1, the width of the sO_2 distribution increased slightly and the median values shifted slightly toward higher sO_2 values (Table 2).

Tumor HI-3 exhibited a more heterogeneous sO_2 distribution with a peak at high sO_2 values at day 1, which then became broader with an increasing fraction of pixels at low sO_2 values [<40% sO_2, Fig. 4(b)]. While the peak of the tumor did not shift significantly, the fraction of low sO_2 pixels changed considerably with time. Figure 4(e) illustrates the sO_2 distributions of the same tumor when the animal was breathing 100% O_2 rather than air. This tumor exhibited an increased heterogeneity as compared to the air-breathing condition. Distinct regions of different sO_2 levels can be identified in the respective color maps [Fig. 4(f)]. The strong reduction of pixels with low sO_2 values at day 41 correlates spatially with the occurrence of the central region without PA signal.

Although the volumes of the AT1-tumors increased up to sevenfold in 12 days [Fig. 4(d)], their sO_2 distributions experienced only minor changes in sO_2 medians and 25/75 percentile ranges [Fig. 4(c) and Table 2].

3.4 *Sensitivity of sO_2 Distributions on External Changes in Oxygen Supply*

Figure 5 displays the changes in sO_2 distributions for the three tumor sublines as well as for the skin when changing the external oxygen supply of the animals. For each of the cases, pooled

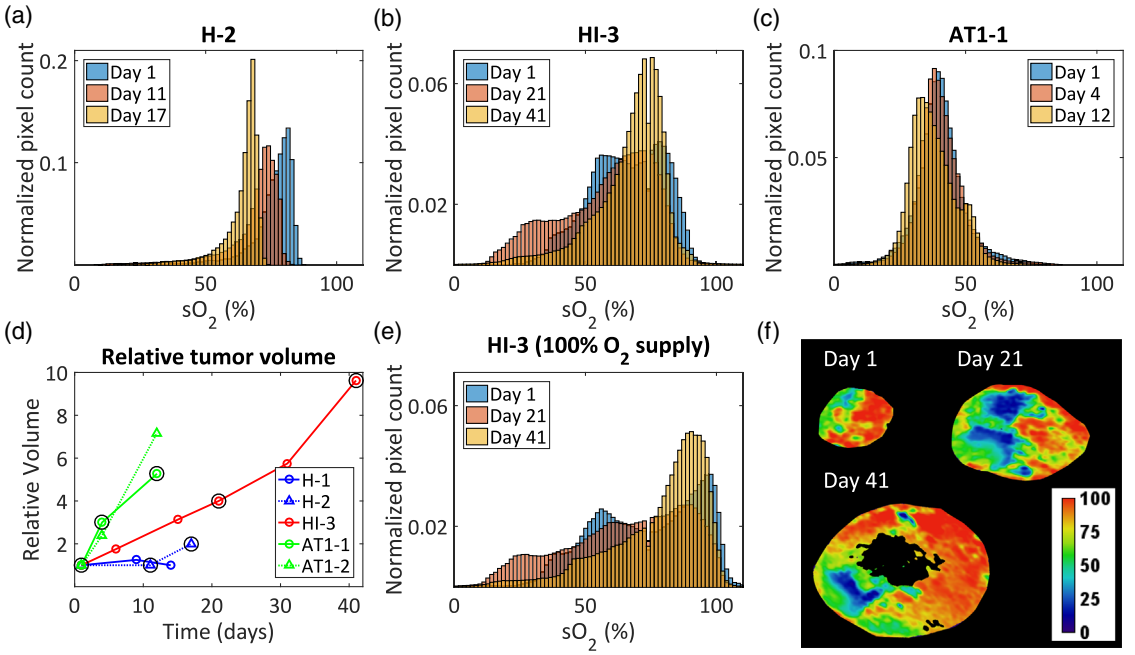

Fig. 4 Temporal changes of the sO_2 distributions for representative tumors of the three sublines: (a) H-2, (b) HI-3, and (c) AT1-1 tumor, imaged when the animals were breathing air. Results at other time points and for additional tumors are given in Table 2. (d) Development of tumor volume with time. As tumor HI-4 was only imaged once, it is not listed in (d). Black circles indicate imaging time points that are depicted in (a)–(c). (e) sO_2 distributions and (f) representative sO_2 color maps of tumor HI-3 when the animal was breathing 100% O_2.

data of two tumors (left column) and one exemplary full experiment performed in a single tumor (middle column) are shown. All medians and 25/75 percentiles are listed in detail in Table 2.

After switching the external gas supply from 100% O_2 to air, the PA signal of the H-tumor immediately shifted to lower sO_2 values while still maintaining its narrow and well-defined peak [Figs. 5(a) and 5(b), Table 2]. When clamping the tumor-supplying arteries, the sO_2 distribution shifted to even lower values, while broadening significantly in spite of the fact that the animals were still breathing 100% O_2. When executing the full oxygen challenge experiment [Fig. 5(b)], the initial sO_2 distributions were restored after switching back from air to 100% O_2 ("100% O_2 post") and after releasing the clamping ("100% O_2 postclamping"), respectively.

When changing the external oxygen supply from 100% O_2 to air, the broad sO_2 distributions of the HI-tumors were shifted to lower values [Figs. 5(c) and 5(d)]. Clamping of tumors led to further shift and broadening of the peak. Again, when performing the full oxygen challenge experiment [Fig. 5(d)], the initial sO_2 distributions were essentially restored after switching back from air to 100% O_2 and after releasing the clamping, respectively.

In contrast to the H- and HI-tumors, essentially no differences were detected for the sO_2 distributions of the AT1-tumors after switching from 100% O_2 to air and after clamping [Figs. 5(e) and 5(f)].

The skin showed a broad distribution at high sO_2 values when the animals were breathing 100% O_2 [Figs. 5(g) and 5(h)]. When switching to air, the peak of the distribution was shifted to lower sO_2 and clamping led to a further significant shift and broadening of the distributions. Again, when performing the full oxygen challenge experiment [Fig. 5(h)], the initial sO_2 distributions were essentially restored after switching back from air to 100% O_2 and after releasing the clamping, respectively.

Changes of the sO_2 distributions during the oxygen challenge experiment were quantified by the similarity measure EMD (Fig. 6). Using the first measurement, where animals were breathing 100% O_2, as a reference, it can be clearly seen that all other measurements with 100% O_2 exhibit very low EMD values (i.e., high similarity), while air breathing and even more clamping exhibited much larger values (decreasingly low similarity). The AT1-tumor on the other hand showed no response to any external changes and their EMDs remained below 0.05 for all experiments.

3.5 *Histology and Immunohistochemistry*

Figure 7 displays representative stainings of the investigated tumors. The H-tumor showed to be highly differentiated with glandular structures comparable to normal prostate glands [Fig. 7(a)] and exhibited mature vessels [Figs. 7(d) and 7(g)]. The whole tumor was well perfused, indicated by a uniformly distributed Hoechst staining. Both H-tumors exhibited only a small, locally confined hypoxic region [Fig. 7(d)] with an increased CAIX expression [Fig. 7(j)]. Apart from those locally confined areas, both tumors were negative for pimonidazole and CAIX.

The moderately differentiated HI-tumor contained mucin secreting glandular structures [Fig. 7(b)] with immature vessels, though not all of them were perfused [Figs. 7(e) and 7(h)]. Hypoxic areas were found to enclose vessels in a certain distance [Fig. 7(h)]. CAIX expression overlapped nearly completely with hypoxic areas [Fig. 7(k)].

Table 2 Summary of oxygen challenge and clamping experiments for tumors and skin. Results are displayed as median and 25/75 percentiles for each tumor and skin for each oxygenation condition.

Animal	Day	Size (mm^3)	100% O_2 pre	Air	100% O_2 post	100% O_2 clamped	100% O_2 postclamping
H-tumor							
H-1	Day 1	40		68 [65, 71]			
	Day 9[a]	50	93 [87, 97][b]	73 [70, 76][b]	96 [91, 99]	57 [48, 68][b]	96 [91, 98]
	Day 14	40	84 [75, 92]	76 [69, 81]	85 [75, 93]	36 [29, 42]	97 [92, 100]
H-2	Day 1	20	92 [88, 96]	78 [74, 81]			
	Day 11	20	94 [89, 97][b]	72 [67, 75][b]		50 [42, 58][b]	
	Day 17	40		66 [62, 68]			
HI-tumor							
HI-3	Day 1	80	75 [57, 91]	66 [56, 77]		30 [21, 45]	87 [62, 96]
	Day 6	140	92 [73, 97]	82 [64, 82]	91 [76, 96]	25 [18, 41]	96 [76, 96]
	Day 15	250	83 [60, 94]	68 [53, 78]	73 [53, 88]	23 [15, 43]	83 [60, 94]
	Day 21[a]	320	69 [49, 85]	61 [45, 72]	70 [53, 85]	37 [29, 50]	74 [54, 89]
	Day 31	460	85 [71, 93][b]	72 [60, 79][b]	82 [64, 91]	43 [35, 55][b]	73 [54, 89]
	Day 41	770	84 [68, 91]	70 [61, 76]	79 [67, 88]	28 [18, 47]	79 [66, 90]
HI-4[c]	Day 1	580	85 [82, 91]	71 [64, 74]		25 [17, 35]	87 [81, 93]
AT1-tumor							
AT1-1	Day 1	110	40 [35, 46]	40 [36, 45]	41 [36, 47]	43 [35, 50]	43 [38, 49]
	Day 4[a]	330	41 [36, 47][b]	40 [36, 45][b]	42 [37, 49]	42 [37, 46][b]	40 [36, 44]
	Day 12	580	37 [31, 44]	37 [32, 43]	38 [32, 45]	40 [30, 48]	42 [36, 49]
AT1-2[d]	Day 1	460	42 [35, 49][b]	40 [32, 48][b]			
	Day 4	1100	45 [38, 51]	46 [39, 52]			
	Day 12	3300	45 [39, 51]	44 [38, 51]			
Skin							
Skin-1	—	—	83 [69, 92][b]	67 [56, 75][b]	77 [63, 86]	16 [12, 22][b]	63 [53, 73]
Skin-2[a]	—	—	82 [67, 91][b]	69 [58, 77][b]	78 [66, 87]	18 [12, 27][b]	84 [73, 90]

[a]Distributions displayed in Fig. 5 middle column.
[b]Data included in pooled distributions in Fig. 5 left column.
[c]Animal could only be imaged once due to scab formation on the skin.
[d]Location of the tumor did not allow clamping experiments.

The anaplastic AT1-tumor exhibited only capillaries, but no mature vessels and showed to be completely undifferentiated without any prostate-specific cells [Fig. 7(c)]. The entire tumor was pervaded by very short and thin capillaries of which only a minority was perfused [mainly at the periphery of the tumor; Figs. 7(f) and 7(i)]. Additionally, prominent hypoxic areas were found [Figs. 7(f) and 7(i)]. The entire AT1-tumor expressed CAIX, with slightly stronger expression at the border of hypoxic areas [Fig. 7(l)].

4 Discussion

PAI is gaining increased interest for preclinical and clinical applications especially in the field of oncology.[1–3,8,23–26] While many preclinical PAI studies on oxygen saturation provide only ROI-based mean values,[27–30] others have developed more advanced imaging and analysis protocols using multispectral PAI.[23,24,31] First approaches for pixel- rather than ROI-based analyses were introduced by May et al.[32] and Hysi et al.[33] In the present study, we extended their approaches

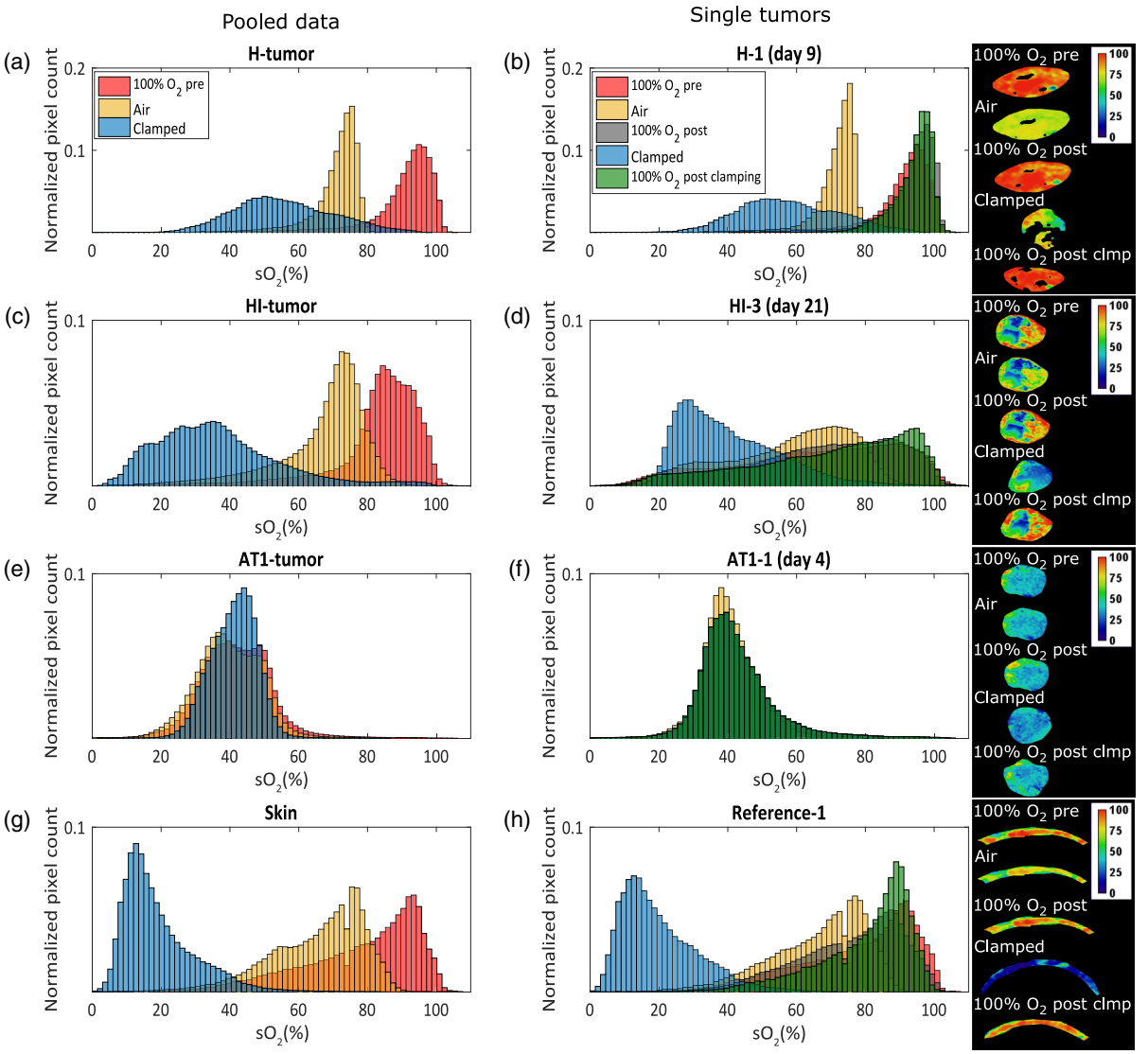

Fig. 5 Oxygen challenge and clamping experiment for each of the three sublines and the skin (reference tissue). Pooled sO_2 distributions per subline and exemplary distributions of the full experiment for single animals: The left column displays the pooled sO_2 distributions of two tumors of comparable volumes of the subline: (a) H (20 and 50 mm^3), (c) HI (460 and 580 mm^3), (e) AT1 (330 and 460 mm^3, for the "clamped"-measurement, the distribution represents only AT1-1), and (g) the skin. Exemplary full oxygen challenge experiments performed in a single tumor per subline are shown in the middle column [(b), (d), (f), (h)]. The right column displays representative frames from 3-D PA sO_2 measurements, which illustrate the characteristics of the response of the tumors after external changes in O_2 supply. Note the highly nonuniform response of the HI-tumor exhibiting regions without changes during oxygen challenge (e.g., low sO_2 region in the center of the tumor) and responding regions in the periphery of the tumor (with high initial sO_2).

to gain pixel-based sO_2 distributions of the entire 3-D tumor volume.

The established protocol enables us to characterize the tumor sublines H, HI, and AT1 of the experimental prostate tumor model Dunning R3327 based on their sO_2 distributions and their response after external changes of oxygen supply. Furthermore, we can investigate whether this response occurs within the entire tumor or only locally and whether this behavior is changing with time indicating morphological or functional changes within the tumor. This detailed analysis would not be feasible, if only mean values per tumor were considered.

The study was conducted using two commercial PAI-systems: the Vevo 2100 and Vevo 3100, both employing the laser Vevo-LAZR. According to the manufacturer, the two systems are broadly comparable with respect to system electronics and PA-specific performance (penetration depth, system dynamic range, signal-to-noise ratio, contrast sensitivity). Therefore, the resulting sO_2 distributions should not be affected by the choice of the PAI system.

4.1 *Dependency of sO_2 Distibutions on Signal Gain and Threshold*

As expected, the resulting sO_2 distributions were mostly independent of signal gain, applied threshold, and positioning of the animals. The higher variability of the sO_2 distributions

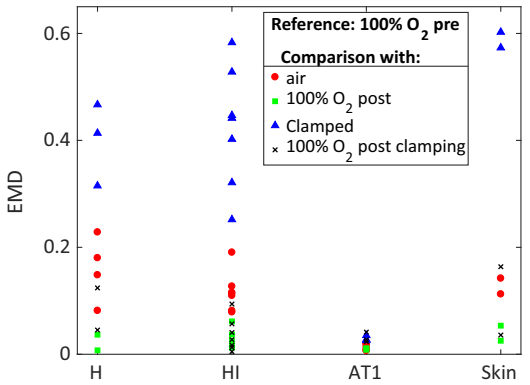

Fig. 6 The similarity measure EMD for the oxygen challenge experiment: The EMD was calculated for all sO_2 distributions measured for the three tumor sublines and the skin using the sO_2 distributions of the first measurement with 100% O_2 ("100% O_2 pre") as reference.

observed for HI-2 can be explained by the overall weak PA signal as the low number of pixels that remained after thresholding cannot be considered as being representative for the tumor. Hence, we decided to adjust the signal gain individually per animal and imaging session taking the strong and distinct PA signal of the well-oxygenated healthy skin as reference. This approach is justified by the fact that tumors were always transplanted at the same location according to a fixed protocol while environmental factors, such as RT, temperature of animal heating table, and gel temperature, were kept constant. Based on these measures, the skin can be considered as reliable and reproducible reference tissue for the selection of individual measurement parameters.

4.2 *Characterization of Tumor Sublines, Temporal Changes, and Response to External Changes in Oxygen Supply*

The three tumor sublines H, HI, and AT1 are know to differ with respect to several parameters, most important the oxygenation status.[10,34,35]

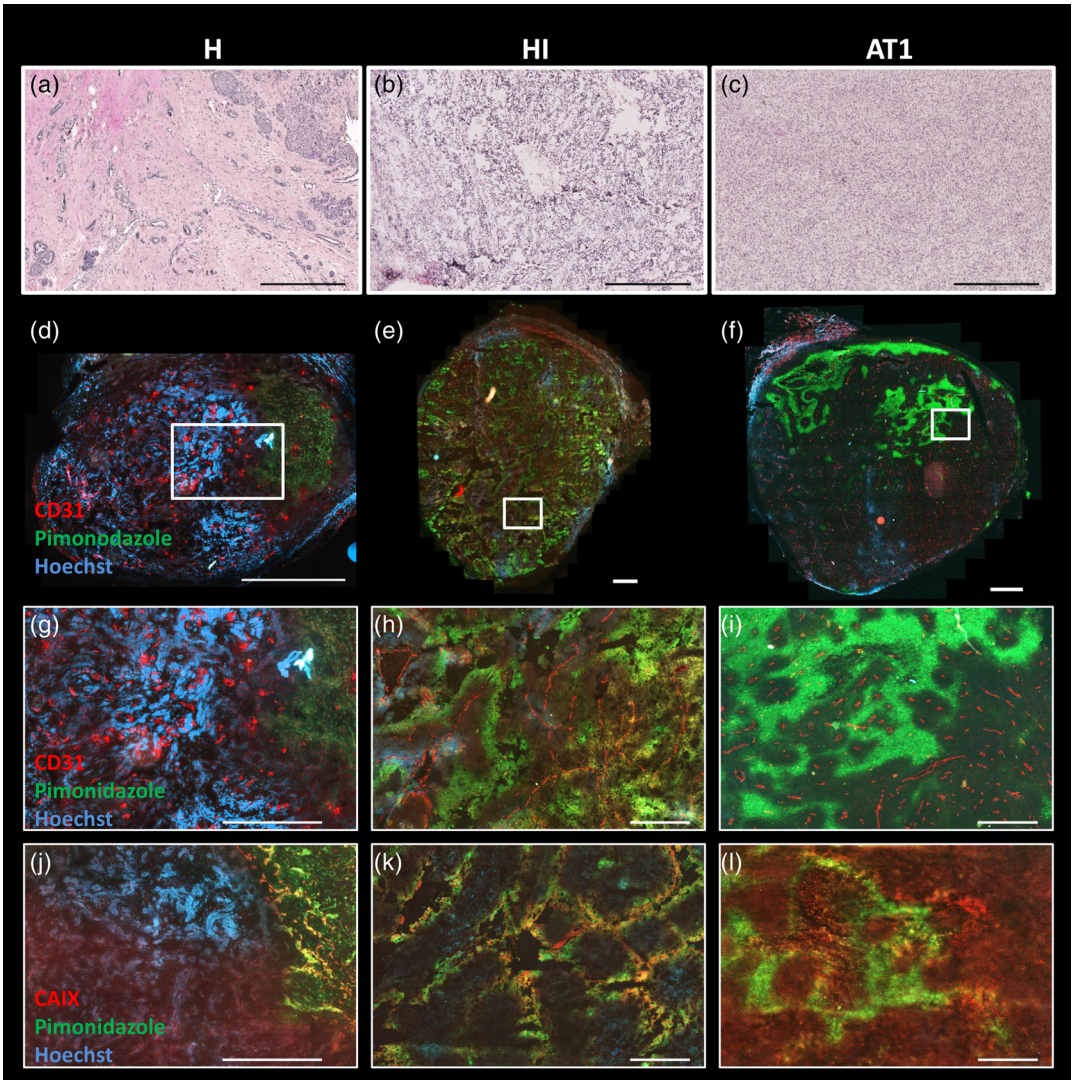

Fig. 7 Histology and immunofluorescence results of the H-, HI,- and AT1-tumor sublines (left, middle and right column, respectively): (a–c) H&E stainings, (d–f) immunofluorescence stainings for vessels (CD31 in red), hypoxia (pimonidazole in green), and perfusion (Hoechst in blue), (g–i) close-ups of the marked areas in (d–f), (j–l) immunofluorescence stainings for CAIX expression (red), hypoxia (green), and perfusion (blue). Scale bars: (a–c), (g–l): 500 μm, (d–f): 1000 μm.

The highly differentiated and slowly growing H-tumor is most similar to normal prostate tissue. The narrow peaks of the sO_2 distributions at high sO_2 values indicate homogenously oxygenated tumors, which were confirmed by immunohistochemistry (IHC), revealing mature vessels ensuring a sufficient blood supply. The shape of the sO_2 distributions was maintained during the observation period without developing a shoulder at lower sO_2 values as found for the HI-tumor.

In addition, PAI was sensitive enough to detect the acute changes in oxygenation induced by changing the breathing gas from 100% O_2 to air as well as by clamping and the response of different animals was highly uniform. A similar finding was described by Zhao et al.[36] The small hypoxic fraction found in IHC stainings of the H-tumors is also in accordance with previously published work[37] and is negligible in comparison to the other sublines.

The sO_2 distributions of small HI-tumors exhibited narrow sO_2 peaks comparable to those of the H-tumors but showed an additional shoulder in the low sO_2 region. HI-tumors are known to develop hypoxia with time,[37] which was also confirmed by the IHC staining and by the increasing fraction of low-sO_2 pixels during the long-term temporal observation. The immediate response to external changes in oxygen supply and the presence of responding and nonresponding tumor regions has also been described by Zhao et al.[38] Tumor HI-3 especially illustrates the potential of the established protocol: During the 41 days of observation, this tumor underwent major morphological changes, which were reflected by the changing shapes of the corresponding sO_2 distributions. This makes the developed protocol especially interesting for longitudinal studies (e.g., after treatment), where changes in oxygenation are expected.

The anaplastic AT1-tumor exhibited narrow peaks in the low sO_2 region, which remained essentially unchanged with respect to time point and oxygenation conditions (EMD < 0.05 for all comparisons). IHC staining revealed that the immature and hardly perfused capillaries could not sufficiently supply the AT1-tumors, which explains the chronically low sO_2 values.[37] While the results of the oxygen challenge experiment are in accordance with those of Mason et al.[39] and Zhao et al.,[36] other investigators found a very small but statistically significant change in perfusion after changing the external oxygen supply from 100% O_2 to air.[40] As our results were reproducible over a period of 12 days and since the comparison of different tumor sublines is based on measurements performed on the same day, any PAI system-related artifacts can be ruled-out.

Considering the different responses of the tumor sublines, PAI measurements performed during oxygen challenge experiments may be a suitable method to differentiate chronic from acute hypoxic tumors (e.g., H/HI versus AT1).

4.3 *Comparison of Tumor Sublines and Normal Tissue (Skin)*

Changing the breathing gas from 100% O_2 to air showed comparable responses in sO_2 distributions of the H- and HI-tumors as well as the normal tissue (skin). Similar results were found by Smith et al.,[41] who investigated the response of several vessel types to different breathing conditions by PAI. Using clamping, tumors and normal tissue showed different responses in our study: while the skin was strongly affected by the acute hypoxic situation, showing a dramatic decrease in sO_2, the distributions of the H- and HI-tumors were shifted to less extreme sO_2 values after clamping, however, the distributions were significantly broadened. The different responses of normal tissues and tumors suggest that the clamping method reduces perfusion uniformly to very low sO_2 values in normal tissue but to very different degrees in different areas of the tumor. The reason for this may be the irregular and chaotic vascular structure of tumors as well as the less clearly defined access of tumor vessels to the large normal arteries. Another possible hypothesis could be a different adaption of tumor and normal cells to oxygen changes leading to various sO_2 changes depending on the tissue composition and the level of dedifferentiation of tumor cells.

For detailed biological investigation of tumor hypoxia, the small number of animals per subline may be considered as a limitation. The main purpose of this study, however, was to establish the quantitative pixel-based PAI method to measure the oxygenation status of experimental tumors. Using three different tumor models with different characteristics, we demonstrated suitability, sensitivity, and feasibility of the established protocol. In the future, multimodal imaging studies may allow further validation of this PAI method and may also generate complementary data allowing for a more complete characterization of the tumors.

5 Conclusion

In conclusion, the presented PAI approach allows displaying sO_2 distributions of entire tumor volumes and hence offers the possibility of a more detailed analysis of the tumors' sO_2 profiles. Derived distributions showed to be independent from signal gain and threshold and they reliably reflected temporal changes in oxygenation of the H-, HI-, and AT1-tumor after external changes of oxygen supply. Therefore, this approach is especially interesting for monitoring changes in tumor oxygenation in response to radiation treatments, where reoxygenation is known to be an important predictor for outcome.[42]

Disclosures

The authors disclose no potential conflicts of interest.

Acknowledgments

This work was supported by the German Research Foundation (Grant Nos. DFG, GL 893/1-1 and KA2679/3-1). The support of the Center for Preclinical Research and the Small Animal Imaging core facility of the DKFZ is greatly acknowledged.

References

1. K. E. Wilson et al., "Spectroscopic photoacoustic molecular imaging of breast cancer using a B7-H3-targeted ICG contrast agent," *Theranostics* **7**(6), 1463–1476 (2017).
2. L. V. Wang, "Prospects of photoacoustic tomography," *Med. Phys.* **35**(12), 5758–5767 (2008).
3. M. Mehrmohammadi et al., "Photoacoustic imaging for cancer detection and staging," *Curr. Mol. Imaging* **2**(1), 89–105 (2013).
4. P. Beard, "Biomedical photoacoustic imaging," *Interface Focus* **1**(4), 602–631 (2011).
5. C. Li and L. V. Wang, "Photoacoustic tomography and sensing in biomedicine," *Phys. Med. Biol.* **54**(19), R59–R97 (2009).
6. J. L. Tatum et al., "Hypoxia: importance in tumor biology, noninvasive measurement by imaging, and value of its measurement in the management of cancer therapy," *Int. J. Radiat. Biol.* **82**(10), 699–757 (2006).
7. K. A. Krohn, J. M. Link, and R. P. Mason, "Molecular imaging of hypoxia," *J. Nucl. Med.* **49**(Suppl 2), 129S–148S (2008).

8. A. Becker et al., "Multispectral optoacoustic tomography of the human breast: characterisation of healthy tissue and malignant lesions using a hybrid ultrasound-optoacoustic approach," *Eur. Radiol.* **28**(2), 602–609 (2018).
9. X. Wang et al., "Noninvasive imaging of hemoglobin concentration and oxygenation in the rat brain using high-resolution photoacoustic tomography," *J. Biomed. Opt.* **11**(2), 024015 (2006).
10. J. T. Isaacs et al., "Animals models of the hormone-sensitive and -insensitive prostatic adenocarcinomas, Dunning R-3327-H, R-3327-HI, and R-3327-AT," *Cancer Res.* **38**, 4353–4359 (1978).
11. C. Glowa et al., "Carbon ion radiotherapy decreases the impact of tumor heterogeneity on radiation response in experimental prostate tumors," *Cancer Lett.* **378**(2), 97–103 (2016).
12. A. Needles et al., "Development and initial application of a fully integrated photoacoustic micro-ultrasound system," *IEEE Trans. Ultrason. Ferroelectr. Freq. Control* **60**(5), 888–897 (2013).
13. W. S. Rasband, *ImageJ*, U. S. National Institutes of Health, Bethesda, Maryland (1997–2016).
14. S. Prahl. "Optical absorption of hemoglobin," 1999, http://omlc.ogi.edu/spectra/hemoglobin/index.html (17 July 2017).
15. L. Wasserstein, "Markov processes on countable product space, describing large systems of automata," *Problemy Peredachi Informatsii* **5**(3), 64–73 (1969).
16. S. S. Vallender, "Calculation of the Wasserstein distance between probability distributions on the line," *Theor. Probab. Appl.* **18**(4), 784–786 (1974).
17. A. M. Vershik, "Long history of the Monge-Kantorovich transportation problem," *Math. Intell.* **35**(4), 1–9 (2013).
18. M. Sommerfeld and A. Munk, "Inference for empirical Wasserstein distances on finite spaces," *J. R. Stat. Soc. Ser. B-Stat. Methodol* **80**(1), 219–238 (2018).
19. Y. Rubner, C. Tomasi, and L. J. Guibas, "The Earth mover's distance as a metric for image retrieval," *Int. J. Comput. Vis.* **40**(2), 99–121 (2000).
20. L. Oudre et al., "Classification of periodic activities using the Wasserstein distance," *IEEE Trans. Biomed. Eng.* **59**(6), 1610–1619 (2012).
21. A. Munk and C. Czado, "Non-parametric validation of similar distributions and assessment of goodness of fit," *J. R. Stat. Soc. Ser. B-Stat. Methodol.* **60**, 223–241 (1998).
22. P. Qiu, "Inferring phenotypic properties from single-cell characteristics," *PLoS One* **7**(5), e37038 (2012).
23. G. C. Langhout et al., "Detection of melanoma metastases in resected human lymph nodes by noninvasive multispectral photoacoustic imaging," *Int. J. Biomed. Imaging* **2014**, 1–7 (2014).
24. G. P. Luke and S. Y. Emelianov, "Label-free detection of lymph node metastases with US- guided functional photoacoustic imaging," *Radiology* **277**(2), 435–442 (2015).
25. J. Laufer et al., "Three-dimensional noninvasive imaging of the vasculature in the mouse brain using a high resolution photoacoustic scanner," *Appl. Opt.* **48**(10), D299–D306 (2009).
26. X. Wang et al., "Noninvasive laser-induced photoacoustic tomography for structural and functional in vivo imaging of the brain," *Nat. Biotechnol.* **21**(7), 803–806 (2003).
27. L. J. Rich and M. Seshadri, "Photoacoustic monitoring of tumor and normal tissue response to radiation," *Sci. Rep.* **6**, 21237 (2016).
28. J. R. Eisenbrey et al., "Comparison of photoacoustically derived hemoglobin and oxygenation measurements with contrast-enhanced ultrasound estimated vascularity and immunohistochemical staining in a breast cancer model," *Ultrason. Imaging* **37**(1), 42–52 (2015).
29. S. Mallidi et al., "Prediction of tumor recurrence and therapy monitoring using ultrasound-guided photoacoustic imaging," *Theranostics* **5**(3), 289–301 (2015).
30. F. Raes et al., "High resolution ultrasound and photoacoustic imaging of orthotopic lung cancer in mice: new perspectives for onco-pharmacology," *PLoS One* **11**(4), e0153532 (2016).
31. C. L. Bayer, G. P. Luke, and S.Y. Emelianov, "Photoacoustic imaging for medical diagnostics," *Acoust. Today* **8**(4), 15–23 (2012).
32. J. P. May et al., "Photoacoustic imaging of cancer treatment response: early detection of therapeutic effect from thermosensitive liposomes," *PLoS One* **11**(10), e0165345 (2016).
33. E. Hysi et al., "Photoacoustic signal characterization of cancer treatment response: correlation with changes in tumor oxygenation," *Photoacoustics* **5**, 25–35 (2017).
34. J. K. Smolev et al., "Characterization of the Dunning R3327H porstatic adenocarcinoma: an appropriate animal model for prostatic cancer," *Cancer Treat. Rep.* **61**(2), 273–287 (1977).
35. T. R. Tennant et al., "The Dunning model," *Prostate* **43**, 295–302 (2000).
36. D. Zhao et al., "Tumor oxygen dynamics: correlation of in vivo MRI with histological findings," *Neoplasia* **5**(4), 308–318 (2003).
37. P. Mena-Romano et al., "Measurement of hypoxia-related parameters in three sublines of a rat prostate carcinoma using dynamic (18)F-FMISO-PET-CT and quantitative histology," *Am. J. Nucl. Med. Mol. Imaging* **5**(4), 348–362 (2015).
38. D. Zhao et al., "Differential oxygen dynamics in two diverse Dunning prostate R3327 rat tumor sublines with respect to growth and respiratory challenge," *Int. J. Radiat. Oncol. Biol. Phys.* **53**(3), 744–756 (2002).
39. R. P. Mason et al., "Regional tumor oxygenation and measurement of dynamic changes," *Radiat. Res.* **152**(3), 239–249 (1999).
40. Z. Zhang et al., "Assessment of tumor response to oxygen challenge using quantitative diffusion MRI in an animal model," *J. Magn. Reson. Imaging* **42**(5), 1450–1457 (2015).
41. L. M Smith, J. Varagic, and L. M. Yamaleyeva, "Photoacoustic imaging for the detection of hypoxia in the rat femoral artery and skeletal muscle microcirculation," *Shock* **46**(5), 527–530 (2016).
42. D. Zips et al., "Exploratory prospective trial of hypoxia-specific PET imaging during radiochemotherapy in patients with locally advanced head-and-neck cancer," *Radiother. Oncol.* **105**(1), 21–28 (2012).

Alina L. Bendinger has been a PhD student in the Division of Medical Physics in Radiology at the German Cancer Research Center (DKFZ) in Heidelberg since 2016. She holds a BSc degree in medical physics and a MSc degree in biomedical technologies. During her PhD, she is working on the assessment of tumor hypoxia by multimodal imaging.

Christin Glowa studied biology at the Universities of Bayreuth and Würzburg in Germany. In December 2013, she obtained her PhD degree at the University of Heidelberg, which was awarded with the 16th Christoph Schmelzer Prize. Since then, she has been a postdoc in the Department of Medical Physics in Radiation Oncology at the DKFZ and the University Hospital Heidelberg working on animal experiments for heavy ion radiobiology research especially in the field of carbon ions and hypoxia.

Jörg Peter received his PhD in biomedical engineering from Dresden University of Technology. Following postdoctoral research fellowships at Duke University and Macquarie University, he is currently working at DKFZ Heidelberg. His work centers on the physics of nuclear and optical imaging systems as well as on the development of mathematical and statistical models for image reconstruction, system simulation, tracer and molecular kinetic modeling.

Christian P. Karger works as a medical physicist at German Cancer Research Center (DKFZ) and is an associate professor at the Medical Faculty of the University of Heidelberg. His fields of research are ion beam radiotherapy, quantitative clinical radiobiology, biological modeling, image-guided adaptive radiotherapy, and dosimetry. Recent research activities focus on the response of hypoxic tumors to irradiations with carbon ions and the possibilities of assessing hypoxia in tumors noninvasively by medical imaging.